Large-Displacement Vertical Electrostatic Microactuator Dynamics Using Duty-Cycled Softening/Stiffening Parametric Resonance

Haijun Li, Paul Barnes, Eric Harding, Xiyu Duan, Thomas D. Wang, and Kenn R. Oldham

***Abstract*— Electrostatic microactuators with large vertical scanning range (several hundred micrometers) at high frequency (hundreds to thousands of hertz) and chips' sizes compatible with endoscopic microscopy have recently been demonstrated based on parametric resonance. This paper examines the use and modeling of mixed softening/hardening dynamics to help produce large ranges of motion in this class of mirrors. Origin of spring stiffening behavior in actuator design is described, followed by non-dimensional analysis of actuator motion trends. The experimental results are presented for a sample actuator design with up to 480-μm displacement at 1225 Hz and 60 V. Comparison of predicted trends and comments on benefits and limitations of modeling are provided. [2018-0184]**

***Index Terms*— Microactuators, dynamics, electrostatic devices, biomedical microscopy.**

I. Introduction

THIS paper examines the dynamics of a class of large-displacement, vertical-scanning parametric resonant micro-mirrors. Novel endomicroscopic imaging techniques have generated a demand for a variety of compact scanning micro-mirrors. An increasingly desirable mode of mirror operation is large translational vertical displacement. Mirrors providing such motion can support vertical cross-sectional imaging and/or 3D imaging during single axis confocal, dual axes confocal and multi-photon microscopy, among other applications. Thermal, piezoelectric, and electromagnetic microactuators have previously demonstrated large vertical displacements based on beam bending mechanisms [1]–[5]. However, producing multi-axis scanning with very high frequencies for high frame rate imaging remains difficult for those types of actuation, and complicating nonlinear effects can arise from large deformation bending.

When resonant-only operation is acceptable, electrostatically-actuated micro-mirrors can be preferable, for simple fabrication and large resonant frequencies. Nonetheless, achieving large vertical translation remains challenging. Kiang et al. used a system of vertically-offset comb fingers to produce vertical displacements, but only for tens of microns of displacement [6]. A parametrically-resonant vertical actuator for spectroscopy application achieved very large displacements, but required large chip size and vacuum [7]. Repulsive force [8] and zipper [9] electrostatic actuators have also been proposed, but with still limited range or selection of heights.

Recently, Li et al. demonstrated real-time vertical sectioning with electrostatic micro-mirrors achieving hundreds of microns of displacement in small form factors via parametric resonance [10]–[13]. The largest displacement actuators of this type use an advantageous dynamic response from mixed softening/stiffening behavior of the combined flexure structure and electrostatic forcing under duty-cycled square wave excitation. Experimental demonstrations of this behavior have been published in [11] and [12] while describing endomicroscopic instruments. The dynamics of mixed stiffening and hardening effects that enable this performance, however, have not been analyzed in detail. This paper, then, examines the dynamic modeling and behavior of this class of parametrically-resonant electrostatic scanning mirrors achieving large vertical displacements through mixed stiffening/softening behavior. Performance relative to a selection of other vertical scanning MEMS actuators is compared in Table I.

The phenomenon of parametric resonance has been heavily studied in microelectromechanical systems (MEMS), with applications including electromechanical filters [14], resonators [15], mass sensors [16], micro-mirrors [17], energy harvesters [18], and inertial sensors [19]. Most studies have dealt with systems experiencing small displacements and sinusoidal inputs, with nonlinear behaviors introduced in a variety of ways. The actuators in this work feature significant effects from both stiffening and softening nonlinearities, associated with elastic and electrostatic forcing elements,

Manuscript received August 9, 2018; revised March 16, 2019; accepted April 5, 2019. Date of publication April 26, 2019; date of current version May 31, 2019. This work was supported in part by the National Institutes of Health under Award R01 EB020644 and in part by the National Science Foundation under Award CMMI 1334340. Subject Editor M. Rais-Zadeh. *(Corresponding author: Kenn R. Oldham.)*

H. Li is with the University of Michigan Medical School, Ann Arbor, MI 48109 USA (e-mail: haijunl@umich.edu).

P. Barnes was with the Department of Mechanical Engineering, University of Michigan, Ann Arbor, MI 48109 USA. He is now with the Boeing Company, Seattle, WA 98124 USA.

E. Harding was with the Department of Mechanical Engineering, University of Michigan, Ann Arbor, MI 48109 USA.

X. Duan was with the Department of Biomedical Engineering, University of Michigan Medical School, Ann Arbor, MI 48109 USA. He is now with Apple Inc., Cupertino, CA 95014 USA.

T. D. Wang is with the Department of Biomedical Engineering, University of Michigan Medical School, Ann Arbor, MI 48109 USA, and also with the Department of Mechanical Engineering, University of Michigan Medical School, Ann Arbor, MI 48109 USA (e-mail: thomaswa@umich.edu).

K. R. Oldham is with the Department of Mechanical Engineering, University of Michigan, Ann Arbor, MI 48109 USA (e-mail: oldham@umich.edu).

Color versions of one or more of the figures in this paper are available online at http://ieeexplore.ieee.org.

Digital Object Identifier 10.1109/JMEMS.2019.2911183

TABLE I
COMPARISON OF SELECT MEMS VERTICAL SCANNING ACTUATORS

Source	Transduction	Die Size (mm x mm)	Range (μm)	Frequency (Hz)
Carr [30]	Electrostatic	~1 x 1	10	>100
Milanovic [31]	Electrostatic		24	>1520
Ataman [7]	Electrostatic	~2 x 2	106	1111
Ozdogan [27]	Electrostatic	~4 x 4	86	1200
Jia [32]	Electrothermal	< 2 x 2	480	336
Siu [5]	Electromagnetic	2 x 3	125	215
Zhang [34]	Electromagnetic	3.2 x 3.2	110	600
Xue [29]	Electromagnetic	10 x 10	123	600
Xie [33]	Piezoelectric	~2 x 4	~60	362
Qiu [35]	Piezoelectric	3 x 3	190	280
Choi [3]	Piezoelectric	3.2 x 3.2	500	120
This work	Electrostatic	2.1 x 3.3	480	1225

respectively. These mixed effects appear most rapidly when subject to square wave excitations and are of great importance to achieving the large vertical displacements achieved here.

In early application of parametric resonance analysis to MEMS devices, several studies demonstrated the ability to tune devices to either dominant stiffening or softening behavior [20], [21]. Rhoads et al. comprehensively examined parametric resonant systems subject to both stiffness and forcing nonlinearities and identified mixed stiffening/softening regions of behavior, with results that anticipate those in this work in qualitative behavior [22], [23]. However, these studies examined comparatively small displacements which permitted maximum 3rd-order polynomial fits for both softening and stiffening. Such models cannot fully capture many large deflection capacitance profiles, and analysis was based on pure sinusoidal excitations. Krylov et al. evaluated larger displacement parametric resonance, with a more expansive model for electrostatic nonlinearity, but without additional bifurcations from stiffening effects [24]. Guo et al. designed electrostatic electrodes to exactly produce a specified capacitive forcing function, which could allow full-range dynamics to be analyzed, but for in-plane microactuators [25]. Shahid et al. examined the effects of duty-cycled square wave excitation on parametric resonance of tilting mirrors with large displacements, but these did not exhibit significant spring stiffening effects [26]. Other recent works have examined parametric resonance in repulsive force scanning mirrors [27], examined multiple mode effects [18], and used feedback to initiate parametric resonance [19], [28].

This paper will demonstrate how the interaction between mechanical spring stiffening and electrostatic spring softening effects can produce exceptionally large displacement vertical actuators in small form factor micro-mirrors. Key features include a lumped-parameter spring/lever model for compliance that can be used to calculate stiffening effects in the vertical translational mirrors, examination of key parameters influencing actuator performance, and demonstration of benefits of operation using certain duty cycled square waves. The combination of effects is found to provide enhanced robustness of stable high-gain bifurcations in the system frequency response, at lower voltages than are effective with sinusoidal forcing. Some practical issues related to mirror design and modeling are also discussed.

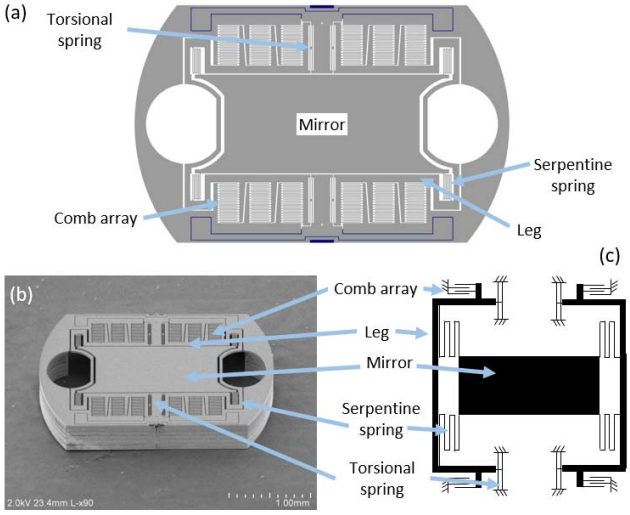

Fig. 1. (a) Mirror layout showing primary design features; (b) scanning electron microscopy image of fabricated mirror; (c) schematic depiction of elements utilized in dynamic mechanical analysis.

II. MIRROR DESIGN

The basic design features of the electrostatic, parametrically-resonant microactuators in this work are a central mirror platform or stage and two or four "leg" structures at which rotation between elastic flexures occurs, shown in a prototype mirror layout, micrograph, and schematic in Fig. 1. Deformation is isolated in the flexures or springs of each leg. One spring is connected to the frame of the device at the leg's base and the other is connected to the central stage at the leg's tip / stage's corner. The remainder of each leg can be considered a rigid beam. The legs also carry the rotor half of the capacitive electrodes or comb fingers that generate electrostatic force. As the central platform moves vertically, the rigid portions of the legs rotate upward, scissors-like.

The central platform may contain an additional fast-axis scanning mirror [10], and the central platform may be subject to resonant vibration modes other than in the vertical direction [10], but this paper will focus on the vertical translational scanning mechanism, which is where dramatic softening-hardening interaction become most significant.

III. MODELING

In vertical motion, the microactuators to be analyzed behave as a nonlinear mass-spring-damping system, with significant nonlinearities arising in the supporting legs (stiffening effect) and electrostatic forcing (softening effect).

A. Spring Stiffening Model

While several phenomena can lead to spring stiffening behavior in MEMS devices, spring stiffening during z-axis translation in the mirrors discussed here arises predominantly from large-deflection mechanics of the leg structures at each corner of the mirror. To analyze spring behavior, we assume symmetric z-axis mirror displacement, with mirror vertical

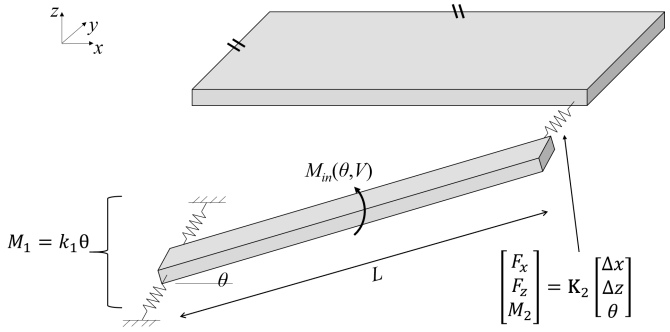

Fig. 2. Schematic model of quarter-mirror structure, assuming symmetric vertical motion and with key flexural elements and dimensions indicated.

displacement z and negligible mirror translation in other axes or rotation.

Vertical motion of the central mirror is produced through out-of-plane rotation of four rigid links, one at each corner of the mirror. To model effective out-of-plane stiffness, consider a rigid link of length L connected at one end to the fixed substrate by a torsion spring, k_1, and at the other end to the mirror platform by a multi-axis spring, $\mathbf{K}_2$, as shown in quarter-mirror schematic of Fig. 2.

Spring behavior at the connection is described by

$$M_1 = k_1\theta \tag{1}$$

where M_1 is the moment applied to the flexure and θ is the rotation angle of the link in the x-z plane. Compliance in off-axis directions at the frame is treated as negligible.

Compliance is designed to be relatively larger at the connection to the mirror, requiring a multi-axis spring model to fully characterize behavior. Under symmetry conditions, the model for the spring connected to the mirror can be described by

$$\begin{bmatrix} F_x \\ F_z \\ M_2 \end{bmatrix} = \mathbf{K}_2 \begin{bmatrix} \Delta x \\ \Delta z \\ \theta \end{bmatrix} = \begin{bmatrix} k_{xx} & 0 & 0 \\ 0 & k_{zz} & k_{z\theta} \\ 0 & k_{\theta z} & k_{\theta\theta} \end{bmatrix} \begin{bmatrix} \Delta x \\ \Delta z \\ \theta \end{bmatrix} \tag{2}$$

where F_x and F_z are lateral and vertical restoring forces between the mirror and leg, M_2 is the restoring moment between the link and mirror, and k_{xx}, k_{zz}, $k_{z\theta}$, $k_{\theta z}$, and $k_{\theta\theta}$ are non-zero components of the spring stiffness matrix given the in-plane spring structure and symmetry of the device. Δx and Δz are the deflection of the spring in the lateral and vertical directions from its neutral position relative to the tip of the leg.

Full derivation of total stiffness of the structure during leg rotation and vertical stage translation is provided in Appendix I. In brief, stiffness simplifies to a relationship between an input moment, M_{in}, on the leg of

$$M_{in} = k_{\theta,tot}\theta + \frac{1}{2!}k_{xx}L^2\theta^3 - \left(\frac{1}{2!3!} + \frac{1}{4!}\right)k_{xx}L^2\theta^5 \tag{3}$$

where $k_{\theta,tot} = k_1 + k_{\theta\theta} - \frac{k_{z\theta}k_{\theta z}}{k_{zz}}$.

In equivalent force terms, for example from a vertical force, F_{in}, applied at the serpentine spring location, (3) can be further summarized as

$$F_{in} \approx \frac{1}{L^2}\left(k_{\theta,tot}z + \frac{1}{2!}k_{xx}z^3\right) \tag{4}$$

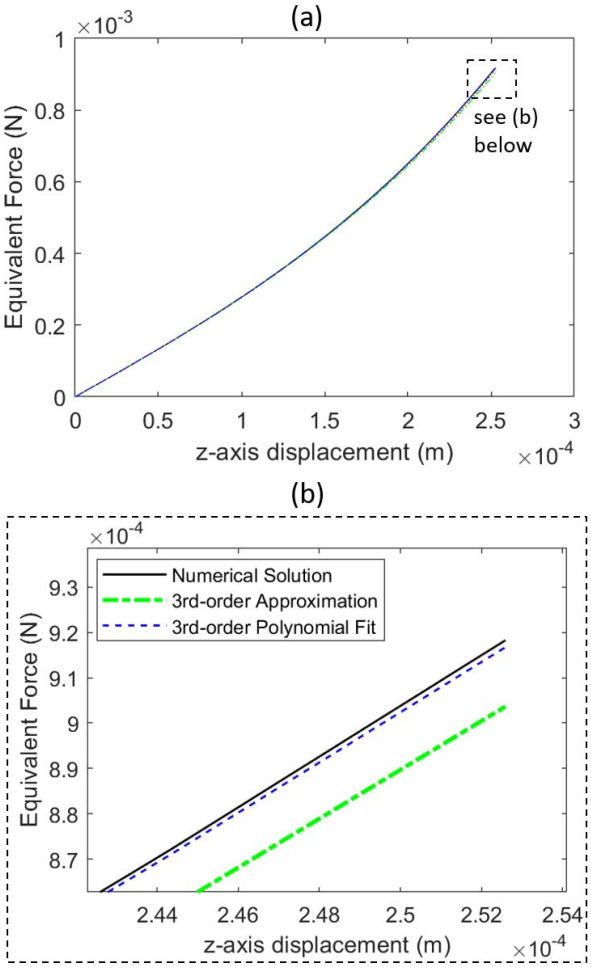

Fig. 3. (a) Modeled force versus displacement curve for the sample vertical scanning mirror; (b) just 1% deviation is observed between a 3rd-order model approximation and the full series expansion of the analytical model over a range of approximately 250 μm, with nominal spring geometry.

An example of the spring stiffening behavior as calculated using a full nonlinear calculation, third order polynomial fit, and series expansion to third order from (3) and (4) is shown in Fig. 3, for leg parameters taken from experimentally-characterized devices as listed in Table II. The stiffening behavior of the leg assembly can be clearly seen. The third-order fit for nonlinear behavior closely approximates the full spring model for central platform displacement up to several hundred microns.

B. Electrostatic Forcing Model

Capacitance between comb fingers on the legs is a function of the rotation angle of the legs, which is nearly proportional to central platform displacement if stiffness k_{zz} is large. As capacitance monotonically decreases with stage displacement and leg angle, polynomial descriptions of capacitance lose accuracy, and alternative descriptions are necessary. Shahid et al. proposed a Gaussian exponential function to describe capacitance [26], and such a model is used in this work. It provides a finite set of parameters to describe

TABLE II
NOMINAL LEG AND MIRROR PARAMETERS FOR REPRESENTATIVE MODEL ANALYSIS

Variable(s)	Label	Units	Value
Equivalent mass	m_{eq}	mg	0.195
Spring stiffnesses	k_1	mN-mm/rad	2.84
	k_{xx}	N/m	28.7
	k_{zz}	N/m	8490
	$k_{z\theta}$	mN/rad	0.064
	$k_{\theta\theta}$	mN-mm/rad	0.14
Leg length	L	mm	0.98
Damping	ξ		0.0065
Capacitance	C_0	pF	13
parameters	β	mm	0.05
	δ	$\sqrt{F}$ x 10^{-6}	2.47
Tested voltages	V		40-60
Dimensionless forcing	η		0.37-0.84
Dimensionless stiffening factor	κ		0.015

capacitive nonlinearity, in the form:

$$C(z) = C_0 + \delta^2 e^{-\frac{z^2}{\beta^2}} \tag{5}$$

where C_0 is a minimum capacitance between structures (including parasitics) and δ and $\beta$are parameters that approximate as a Gaussian curve the roll-off in capacitance that occurs as electrodes move apart. Equivalent forcing generated by the finger arrays is calculated from $\partial C/\partial z$, which gives rise to the equivalent of spring softening behavior as displacement becomes large.

C. System Dynamics

System dynamics can now be summarized using cubic spring stiffening and a derivative of Gaussian function for capacitance. The equation of motion for total stage dynamics in the vertical direction, z, becomes:

$$m_{eq}\frac{d^2z}{dt^2} + c\frac{dz}{dt} + k_{lin}z + k_{cubic}z^3 = -\frac{\delta^2}{\beta^2}ze^{-\frac{z^2}{\beta^2}}V(t)^2 \tag{6}$$

where m_{eq} is the equivalent mass of the mirror and legs in the vertical direction, c is a viscous damping constant, V is input voltage, and k_{lin} and k_{cubic} are the linear and cubic terms in the nonlinear stiffness relationship (i.e., for the stage presented here, $k_{lin} = k_{\theta,tot}/L^2$ and $k_{cubic} = k_{xx}/(L^2 2!)$. m_{eq} is calculated as an equivalent mass with respect to central mirror displacement; to simplify equivalent mass computation, during this step we neglect vertical deformation Δz across $\mathbf{K}_2$, i.e. taking $L\theta \approx z$ when adding inertia, J, of the legs to mirror mass, m.

Under a duty-cycled input, voltage may be rewritten in terms of a binary variable $u(t) = \{0, 1\}$ as $V(t) = V_0 u(t)$, where V is the nominal voltage. At an input frequency ω, corresponding to cycle period $T = 2\pi/\omega$, u is then defined by duty cycle, d, $0 < d < 1$, over periods $n = 0, 1, 2, \ldots$, as

$$u(t) = \begin{cases} 1 & nT < t < nT + dT \\ 0 & nT + dT < t < (n+1)T. \end{cases} \tag{7}$$

Alternatively, under a sine wave input, the input simply becomes $V(t) = V_0 \sin(\omega t)$.

The equation of motion can be non-dimensionalized to

$$\frac{d^2\chi}{d\tau^2} + 2\xi\frac{d\chi}{d\tau} + \chi + \kappa\chi^3 = -\eta\chi e^{-\chi^2}u \tag{8}$$

with dimensionless displacement, χ, and time, τ, defined by

$$\chi = \frac{z}{\beta}, \tag{9}$$

$$\tau = \omega_n t. \tag{10}$$

and having nominal damping ratio $\xi = \frac{c}{2\sqrt{k_{lin}m_{eq}}}$ and nominal natural frequency $\omega_n = \sqrt{\frac{k_{lin}}{m_{eq}}}$. In (8), parameter κ represents the relative strength of cubic stiffening and parameter η represents the dimensionless forcing amplitude,

$$\kappa = \frac{k_{cubic}\beta^2}{k_{lin}} \tag{11}$$

$$\eta = \frac{\delta^2 V_0^2}{\beta^2 k_{lin}}. \tag{12}$$

In addition, dimensionless input frequency can be defined by $\Omega = \omega/\omega_n$. In square wave operation, duty cycle, d, may also be considered a parameter dictating non-dimensional system response, along with Ω, κ, and η.

D. Other Considerations

Beyond z-axis dynamics, as modeled in the previous section, there are several additional design considerations that influence stage performance, though they are not addressed by analytical methods in the current design realization. First, the damping ratio influencing the system must be identified empirically and is known to vary based on the environment in which the actuators and surrounding structures are placed. Second, while in ideal symmetric motion higher-order vibration modes or motions in other axes do not influence vertical translation, in practice asymmetries in the system and un-modeled dynamics can lead to coupling of the vertical parametric resonance with other vibration modes. To avoid this, small displacement resonant frequencies of the mirror structure are identified though linear modal analysis in Ansys finite element analysis software, and candidate mirror designs are rejected if other vibration modes occur at integer multiples of the nominal z-axis resonant frequency. Details of this analysis for a sample mirror used in an endomicroscopy system has been described in [10].

IV. RESULTS

A. Simulation Results

Fig. 4 shows a representative comparison of frequency response plots for the vertical actuators described in this work under sinusoidal and square wave inputs. Parametric resonance in this scenario is excited at approximately twice the nominal mechanical resonant frequency; excitation frequency is shown in frequency response plots, while oscillatory motion occurs at half that frequency, i.e. near $\Omega = 1$. As is common for parametrically-resonant structures, stable resonant

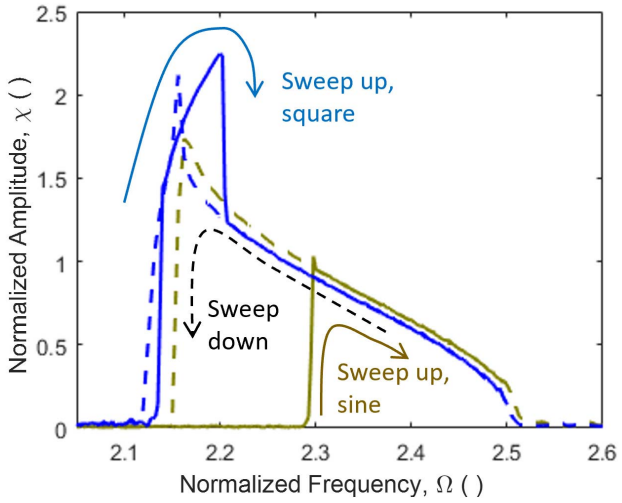

Fig. 4. Sample simulated frequency responses of mixed stiffening-softening dynamics show the extended stable oscillation region during downward frequency sweeping, and secondary bifurcation with high-gain under square wave excitation that is not present under sinusoidal excitation ($\eta = 0.7$, $\kappa = 0.05$, square wave at 50% duty cycle).

behavior is very different when sweeping frequencies from high-to-low (sweep down) versus sweeping from low-to-high (sweep up).

Sweeping down under conditions shown in Fig. 4 ($\xi = 0.02$, $\kappa = 0.05$, $\eta = 0.7$), the response to both a sinusoidal input or 50% square wave is similar, reaching a peak amplitude near $\Omega = 2.1$ for this system, then rapidly dropping to zero as input frequency is reduced further. Sweeping up, however, produces dramatically different results. The sine response remains at equilibrium at the origin until reaching a significantly higher driving frequency than during a sweep down. Square wave excitation, in contrast, returns quickly to stable oscillations, then tracks an additional bifurcation to even higher amplitudes. This additional stiffening-mode bifurcation results in both significantly higher amplitudes than a sinusoidal input with the same input amplitude, and a region of large amplitude resonance that is less sensitive to frequency perturbations than the absolute peak without the stiffening bifurcation present.

Fig. 5 shows a broader sample of frequency sweeps with duty-cycled square waves under various forcing amplitudes and levels of spring stiffening. At low forcing and with only mildly stiffening spring behavior (i.e. $\eta = 0.3$, $\kappa = 0.05$), the high amplitude bifurcation is not observed, but either term becoming stronger can give rise to such an effect. Increased forcing does uniformly increase both the frequency range for which oscillations occur as well as their amplitude, as would be generally expected. Another important observation is that low-duty excitation (for example 30% duty cycle square wave excitation in Fig. 5) produces the largest amplitude oscillations over much of the frequency range of "high-gain" stiffening behavior. This is the opposite of expectations if there were no stiffening present, for which duty cycles greater than 50% provided the broadest range of high-amplitude oscillations in angular rotation based on parametric resonance [26].

B. Theoretical Interpretation

Results in Section IV.B. show representative trends for frequency response of the mixed stiffening-hardening system. From a theoretical perspective, they raise the question as to why high gain behavior appears most readily under low duty cycle square wave excitations when stiffening behavior is present. There are various potential approaches to analyzing a periodically-excited nonlinear system, but for a focus on high-gain behavior we begin with simplifications starting from existing trends in parametrically-resonant systems.

For a parametrically-resonant system under $2n$ excitation (excitation at approximately twice the natural frequency), timing of a square wave input can be characterized as shown in Fig. 6. Dimensionless time τ_1 represents the time period during which the input is 'on' and motion is returning towards its neutral position. With purely attractive (negative forcing), this corresponds to positive work done to the system by the input. Time τ_2 represents the time period when the input is 'off', and zero external work is done by the input. τ_3 represents the time period when the input is 'on' but the system is moving away from its neutral position, corresponding to a period of negative work. Duty cycle is $d = (\tau_1 + \tau_3)/(\tau_1 + \tau_2 + \tau_3)$ and input frequency is $\omega = 2\pi/(\tau_1 + \tau_2 + \tau_3)$ with $\omega \approx 2\omega_n$.

Maximum parametric resonance amplitude is traditionally anticipated if $\tau_3 = 0$ and τ_1 is equal to the periods, for a symmetric system, over which $\chi > 0$, $\frac{d\chi}{d\tau} < 0$ or $\chi < 0$, $\frac{d\chi}{d\tau} > 0$. This maximizes the positive work that is done by the input, exceeding that possible using either a sinusoid or an imperfectly-timed square wave of equal amplitude [17], [26], [36].

In practice, since the system runs open-loop, transition timing is dictated by dynamics in (23) and cannot be set arbitrarily, but large amplitude behavior can still be predicted based on this concept. Consider a pair of state transition functions, Φ_0 and Φ_1 mapping states $\left[\chi \ \frac{d\chi}{d\tau}\right]^T$ forward from a nominal time τ_0 when input $u = 0$ or 1, respectively:

$$\begin{bmatrix} \chi(\tau) \\ \frac{d\chi}{d\tau}(\tau) \end{bmatrix} = \Phi_{0,1}\left(\begin{bmatrix} \chi(\tau_0) \\ \frac{d\chi}{d\tau}(\tau_0) \end{bmatrix}, \tau \right) \tag{13}$$

Candidate limit cycles exist if, over a half cycle of motion from nominal amplitude χ_0 with $\frac{d\chi}{d\tau} = 0$ to $-\chi_0$ with $\frac{d\chi}{d\tau} = 0$, there exist some τ_1, τ_2, and τ_3 satisfying

$$\begin{bmatrix} -\chi_0 \\ 0 \end{bmatrix} = \Phi_1\left(\Phi_0\left(\Phi_1\left(\begin{bmatrix} \chi_0 \\ 0 \end{bmatrix}, \tau_1\right), \tau_2\right), \tau_3\right). \tag{14}$$

(14) may potentially have many solutions, but under the assumption that high amplitude responses feature minimal negative work, or $\tau_3 \approx 0$, (14) can be approximated as satisfied by trajectories satisfying

$$\Phi_0\left(\begin{bmatrix} -\chi_0 \\ 0 \end{bmatrix}, \tau_2\right)^{-1} \approx \Phi_1\left(\begin{bmatrix} \chi_0 \\ 0 \end{bmatrix}, \tau_1\right). \tag{15}$$

Behavior sought in (23) can be visualized graphically in the phase plane. Example are shown in Fig. 7(a,b) for $\kappa = 0$ and $\kappa = 0.2$, respectively, with $\eta = 0.3$. Possible motions from various χ_0 while $u = 1$, i.e. over candidate durations τ_1, are depicted as solid lines from right to left, while motion

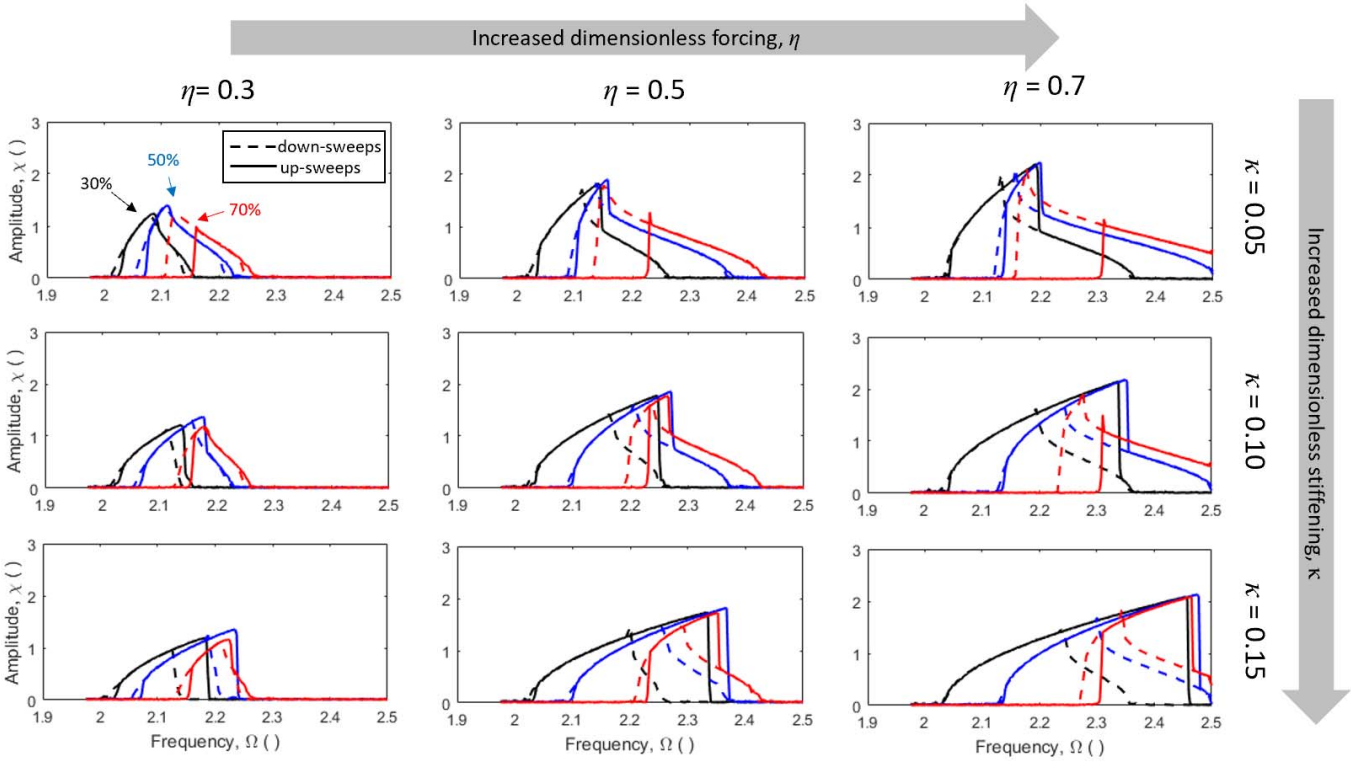

Fig. 5. Trends in simulated non-dimensional, single-sided amplitude of mixed stiffening-hardening micro-scanner dynamics with increasing forcing and stiffening effects at duty cycles of 30%, 50%, and 70% illustrate increased high-gain bifurcation amplitude and frequency range ($\xi = 0.01$).

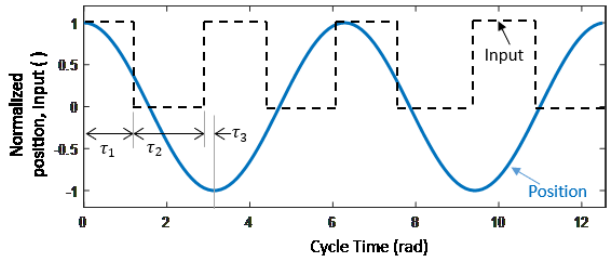

Fig. 6. Schematic motion versus input timing for a duty-cycled square wave. Each half-cycle of motion can be divided into an 'on'-time, labeled τ_1, during which forcing is doing positive work while drawing the system towards its equilibrium, an 'off'-time, τ_2, and an 'on'-time during which forcing is doing negative work, τ_3 as the system moves back away from equilibrium.

while $u = 0$, over candidate durations τ_2, is depicted by dashed lines from left to right from corresponding - χ_0. Candidate 'on'-'off' transition pairs that approximately satisfy (15) are marked, along with phase locations corresponding to $\tau_1 = 30\%$, 50%, and 70% of the nominal input cycle period (i.e. approximately 30%, 50%, and 70% duty cycles). Further perturbation analysis has been performed to distinguish stable from unstable candidate trajectories, though this was not addressed in (13)-(15).

It can be seen that addition of nonlinear forcing substantially increases the range of amplitudes for which candidate limit cycles exist. Furthermore, stable trajectories occur at duty cycles <50%, approaching 50% only near maximum amplitudes with $\chi_0 > 2$, consistent with trends in Fig. 5. Physically, nonlinear stiffness is effectively increasing the velocity with which the system returns towards its nominal equilibrium ($\chi = 0$). This allows motion to be more effectively maintained to an equivalent maximum displacement on the opposite side of a half-cycle while the input is 'off'.

C. Experimental Results

Fig. 8 shows a fabricated micro-mirror utilizing mixed softening/stiffening dynamics. The mirror was fabricated by a two-lithography-mask process from a silicon-on-insulator wafer, as previously described in [12]. For the mirror tested in this paper, the silicon-on-insulator device layer used for the mirror and legs was 50 μm thick, with mirror mass, spring stiffnesses, and leg length determined from the structural geometry, as summarized in Table II. This corresponded to predicted natural frequency $\omega_n = 7330$ rad/s (1170 Hz) and stiffening parameter $\kappa = 0.015$. Total variable capacitance, δ^2, can also be easily calculated from mirror geometry, at 6.1 pF.

Other parameters describing capacitance are more complicated to obtain, due to dependence on the geometry of multiple distributed comb finger arrays and parasitic effects. Full modeling typically requires analysis in computational modeling software, but the Gaussian roll-off parameter β will usually be approximately equal to the device layer thickness, beyond which rotor fingers generate dramatically reduced capacitance. Additional discussion of this point is provided in Section IV.D. Similarly, damping ratio is generally not available analytically, but was estimated at $\xi = 0.0065$ by free oscillatory ring-down testing of mirrors with similar geometry.

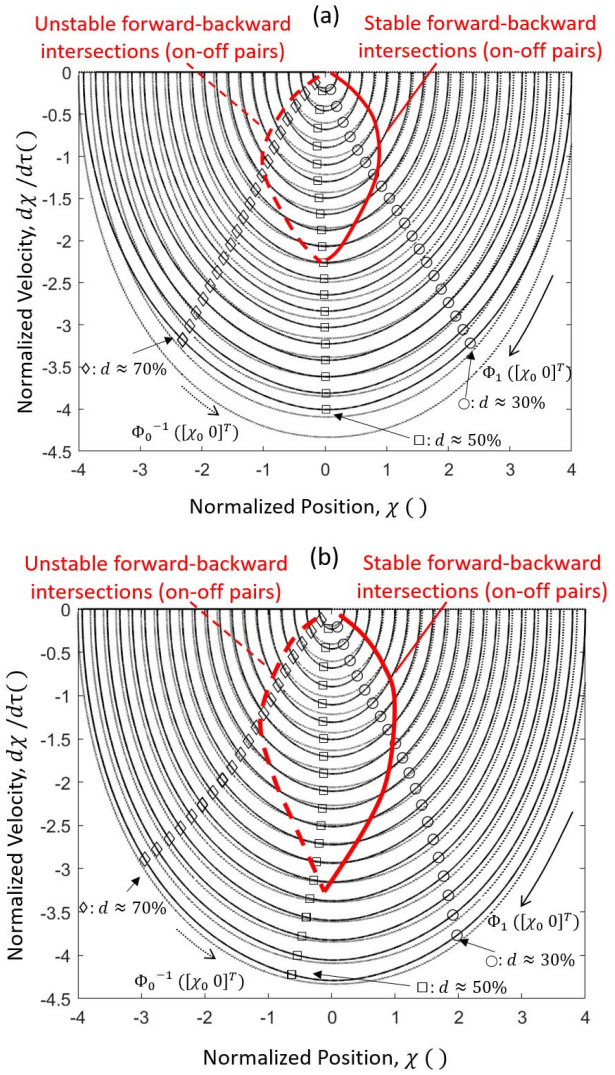

Fig. 7. Phase plots in lower half plane for trajectories of interest in predicting potential oscillatory behavior when (a) $\kappa = 0$ vs (b) $\kappa = 0.2$. Points at which forward trajectories with $u = 1$ (solid lines, starting at right) intersect backward trajectories with $u = 0$ (dashed lines, starting at left) indicate approximate limit cycles when time $\tau_3 \ll \tau_1, \tau_2$, as defined in Fig. 6; perturbation analysis identifies candidate intersections at lower duty cycles as stable during ideal operation.

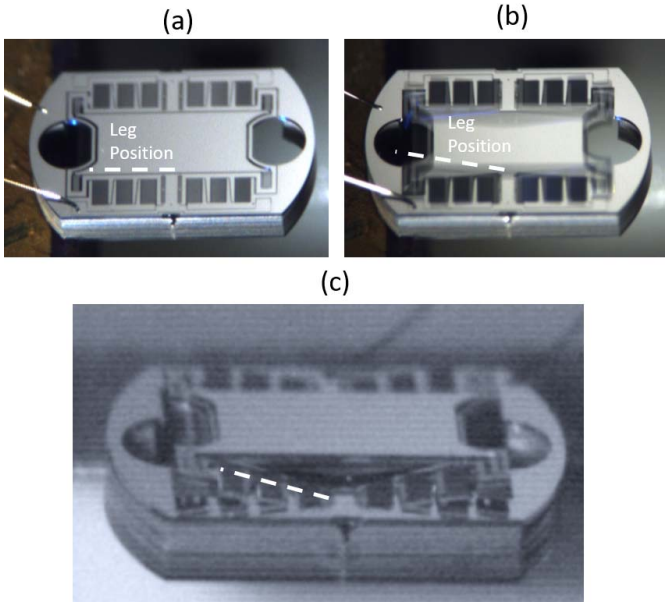

Fig. 8. Sample vertical electrostatic actuator for parametric resonant characterization: (a) mirror after fabrication; (b) optical microscope capture of motion during vertical translational oscillation; (c) freeze frame image acquired with high-speed camera and optical microscope.

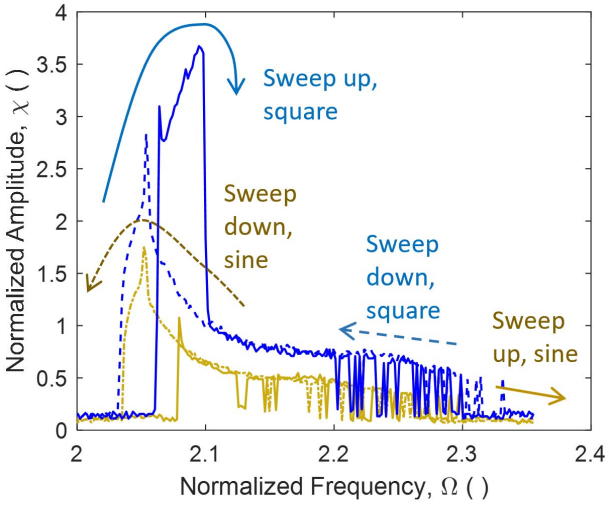

Fig. 9. Experimental frequency response of sample actuator with multiple bifurcations present, in non-dimensional terms, with square wave excitation producing high-gain, stiffening bifurcation not observed at comparable voltages under sinusoidal excitation (50 V/$\eta = 0.58$, 40% duty cycle).

Experimental mirror displacement was measured using translation of a laser reflected onto a photosensor array (PSA). Motion was measured with the PSA at varying distances to ensure that mirror tilt was not contributing to output, and maximum displacement was also examined through optical microscopy and high-speed camera imaging. Maximum displacement measured up to 60 V was 480±30 μm, with maximum tilt angle during vertical translation of <0.1°.

Fig. 9 compares sample response of the mirror to sinusoidal and square wave (40% duty cycle) at 50 V ($\eta = 0.58$), in terms of dimensionless frequency and peak-to-peak amplitude. Again, frequencies shown are driving frequencies, which are twice the frequency of mechanical oscillation. Qualitative agreement is observed between typical model behavior and experimental measurements, as were presented in Fig. 4, with a high-gain region of motion occurring in the up-sweep with a square wave input. We note that data acquisition is sometimes lost in low amplitude motion, due to limitations of the motion tracking algorithm used in our experimental setup.

Figs. 10 and 11 show direct comparisons of experimental and simulated motion, in absolute frequency and peak-to-peak amplitude, for mirror displacement at duty cycles of 20%, 40%, and 60% at 40 V and 50 V. Characteristic mixed hardening/softening behaviors can be seen at 20% and 40% duty cycles, while at larger duty cycles the higher-amplitude bifurcation is not observed either experimentally or in simulation.

Under most conditions, reasonably good agreement between the model and experimental results is obtained. At 20% and 60% duty cycles, error in transition frequency to stable oscillation is less than 10 Hz (approximately 0.4% of the

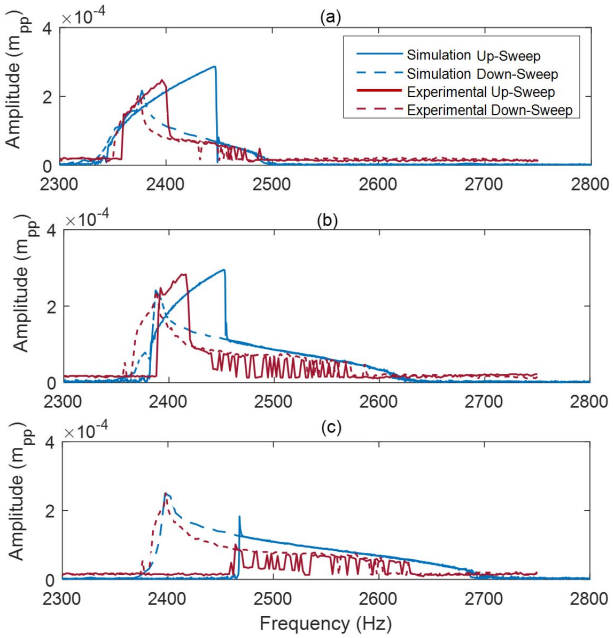

Fig. 10. Comparison of simulated and experimental frequency response, peak-to-peak amplitude with 40 V square wave input ($\eta = 0.37$): (a) 20% duty cycle; (b) 40% duty cycle; (c) 60% duty cycle.

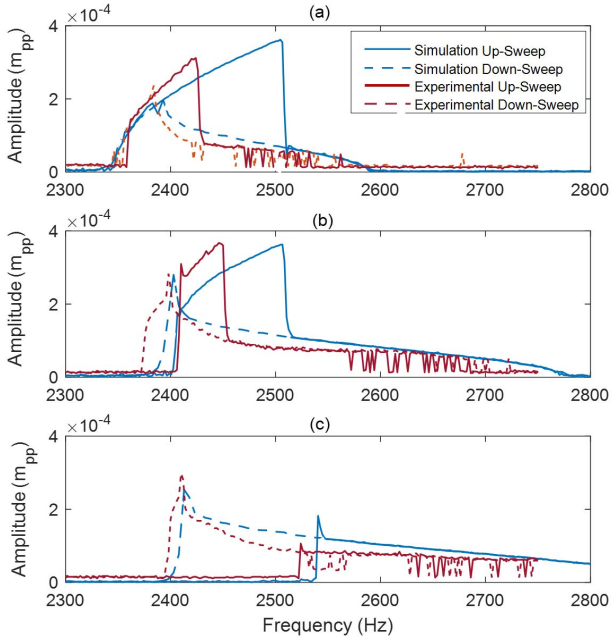

Fig. 11. Comparison of simulated and experimental frequency response, peak-to-peak amplitude with 50 V square wave input ($\eta = 0.58$): (a) 20% duty cycle; (b) 40% duty cycle; (c) 60% duty cycle.

peak oscillation frequency). Mean absolute amplitude error is approximately 15% and maximum absolute amplitude error is 40% at these duty cycles, excluding low-amplitude regions where data acquisition is inconsistent.

The most prominent difference between modeled and experimental data is that the high-amplitude, stiffening bifurcation extends to substantially higher frequencies in simulation than in experiments. Our interpretation is that limit cycles exist theoretically in these regions, but have very small regions of attraction, such that even small perturbations in practice lead to loss of the high-gain oscillatory behavior. In addition, relatively large absolute amplitude differences at highest amplitudes suggest that the Gaussian model for capacitance over-simplifies roll-off of capacitance at large displacements.

Additional discrepancies are present at 40% duty cycle in Fig. 10 and 11 as oscillation terminates during down-sweep excitation. Where a sharp peak is expected in simulation, there is a more gradual transition to the origin in experiments. Again, this is likely in part due to oversimplification of large displacement capacitance, as the initiation of this behavior occurs at some of the larger amplitude motions. However, this does not fully explain the more significant deviation than is seen at 20% or 60% duty cycles, possibly representing further limitations of reducing the capacitance model to a function of two parameters (β and δ).

Reliable mirror operation was found to be possible up to a maximum of 60 V with the mirror design presented here. At this driving voltage, maximum mirror amplitude was obtained experimentally to be 480±30 μm at 2560±30 Hz, 50% duty cycle, and 60 V. Simulated mirror amplitude under these conditions was predicted to reach 440 μm at 2570 Hz. Experience during mirror operation, however, was that mirror motion was less robust at 50% duty cycle than either higher or lower duty cycles. In particular, high-gain stiffening behavior appeared qualitatively less sensitive to operating conditions and exact capacitance and spring parameters at lower duty cycles. Detailed analysis of this aspect of mirror behavior has not been performed at this time.

D. Discussion

For practical use in imaging systems, observed mirror dynamics and successful modeling of behavior have two main benefits. First, at the design stage models may be used to help optimize actuator dimensions. Second, in operation, models can be used in state estimators to improve tracking of mirror and phase near resonance, which can aid in reliable image registration and robustness of operation.

During design, dynamic modeling can be especially helpful in tuning device spring/leg design and, with more effort, capacitance versus angle profiles to target operation near specific frequencies and/or amplitudes; in contrast, mirror or other payload geometry and mass will tend to be dictated by the optical application. The non-dimensional analysis format provides fair flexibility for approximating a variety of spring and comb finger arrays. However, one can anticipate that parametrically-resonant stiffness might exhibit nonlinearity from other locations in other designs, such as by use of alternate spring geometries, in which case the model for spring stiffness versus angle might be incomplete. Other stiffening, or even softening nonlinearities, would remain compatible with non-dimensional analysis trends.

Another limitation of this approach is the capacitance model. Naturally, not all capacitive forcing will be approximated sufficiently accurately by the Gaussian model. Nevertheless, this has benefits for limited tuning parameters

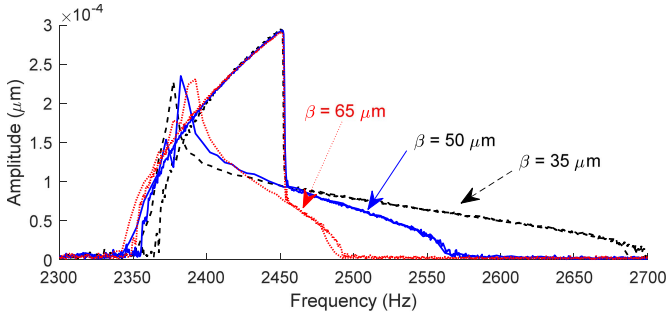

Fig. 12. Varying estimated β parameter can significantly affect low-amplitude oscillation frequencies, but has only a small effect on high-gain amplitude and frequency in simulated response curves.

and capturing diminished capacitance at large displacements. In addition, as noted above best estimates for β can be difficult to obtain. Fundamentally, β is identified by calculating the stage height at which comb array capacitance would decrease by a factor of e^{-1}, but this is complicated by fingers occurring at multiple locations along the legs and fringe capacitances.

Fortunately, peak oscillation amplitudes are relatively insensitive to variation in β alone. This can be observed in Fig. 12. While variation in the softening effect due to β does affect lower amplitude motions, and thus frequencies at which motion is first observed, high-amplitude behavior where stiffening has a major effect (i.e. above 2400 Hz in Fig. 12) is nearly unchanged. We attribute this largely to the dominance of stiffening behavior, dictated by parameter α, in this region. In addition, β has partially offsetting effects on η and κ. Increasing β, for instance, increases nondimensional stiffening κ while decreasing nondimensional forcing η, with opposing effects on total absolute amplitude (though non- dimensional amplitude scaling $\chi = \frac{z}{\beta}$ will depend directly on choice of β).

As a practical matter, in absence of full computational analysis, we have found device layer thickness to be an effective rule-of-thumb for estimating β. Another approximation for β is to calculate the static displacement that reduces capacitance to a 1σ normal distribution height ($\beta = 61$ μm for our geometry). An even a simpler approximation as stage height giving 1/3 reduction in comb area ($\beta = 39$ μm), produced only approximately $\pm 10\%$ variation in simulated oscillation amplitudes in the mixed softening-stiffening region (though much more where only softening is significant).

Finally, the current model does not predict maximum permissible voltage, which is usually limited by lateral off-axis motion of the legs that eventually permits comb finger pull-in as voltage increases. Pull-in may be exacerbated by unwanted excitation of higher-order modes causing interference in comb finger motion. Analysis of higher-order mode interaction and motion in un-modeled axes may provide improved robustness of future mirror designs. Similarly, the regions of convergence about stable bifurcations have not been rigorously evaluated. It is observed experimentally that the highest amplitudes of the spring stiffening bifurcation during upward frequency sweep are very sensitive to perturbations, especially at or above 50% duty cycles.

V. Conclusion

An architecture for vertical scanning micro-mirrors that uses mixed softening and stiffening dynamics to attain large displacements at modest voltages via parametric resonance has been presented. Sample mirrors based on this architecture have achieved up to 480±30 μm vertical displacement in air with a 60 V square wave input, in a chip size of 3.3 mm by 2.9 mm. A model for spring stiffening based on the mirror and actuation geometry is derived. This is combined with a large deflection capacitance model in the equations of motion to examine trends in dynamic mirror behavior under mixed stiffening/softening effects, and to compare experimental results to expected mirror performance. The proposed model should facilitate future micro-mirror optimization, operation, and control. Topics for future analysis include characterization of the region of attraction around stable resonant trajectories, and integration of off-axis or higher-order resonances in modeled spring behavior, with potential benefits for micro-mirror robustness.

Appendix I

Using spring models from (1)-(2), the moment balance for a single link supporting the mirror with respect to an applied external moment, M_{in}, becomes

$$M_{in}(\theta, V) - M_1 - M_2 + F_x L \sin\theta - F_z L \cos\theta = 0 \quad (16)$$

where

$$F_x = k_{xx}(L - L\cos\theta) \quad (17)$$

$$F_z = k_{zz}(z - L\sin\theta) + k_{z\theta}\theta \quad (18)$$

$$M_2 = k_{\theta z}(z - L\sin\theta) + k_{\theta\theta}\theta \quad (19)$$

from the geometric relationship between the end of the link and the mirror position.

In the equations of motion for the system, this produces coupled dynamics in the x-z plane of the form

$$m\ddot{z} + b\dot{z} = -4F_z = -4k_{zz}(\text{z-Lsin}\theta) - 4k_{z\theta}\theta \quad (20)$$

$$\begin{aligned} J\ddot{\theta} + b_\theta\dot{\theta} = {} & -k_1\theta - k_{\theta\theta}\theta - k_{\theta z}(z - L\sin\theta) \\ & + k_{zz}L\cos\theta\,(z - L\sin\theta)\,L\cos\theta + k_{z\theta}L\theta\cos\theta \\ & - k_{xx}(L - Lcos\theta)\,L\sin\theta + M_{in} \end{aligned} \quad (21)$$

In general, this is a nonlinear dynamic system that must be analyzed numerically or by advanced methods. However, the stiffening behavior of this system can be clearly seen in response to a static input moment, when $\ddot{z} = \dot{z} = \ddot{\theta} = \dot{\theta} = 0$, for which (7) and (8) become:

$$0 = -4k_{zz}(z - L\sin\theta) - 4k_{z\theta}\theta \quad (22)$$

$$\begin{aligned} M_{in} = {} & k_1\theta + k_{\theta\theta}\theta + k_{\theta z}(z - L\sin\theta) \\ & - k_{zz}L\cos\theta\,(z - L\sin\theta)\,L\cos\theta - k_{z\theta}L\theta\cos\theta \\ & + k_{xx}(L - Lcos\theta)\,L\sin\theta \end{aligned} \quad (23)$$

Substituting $(\text{z-Lsin}\theta) = -\frac{k_{z\theta}k_{\theta z}}{k_{zz}}$ from (22) into (23), the relationship between leg angle and input moment can be reduced to

$$M_{in} = \left(k_1 + k_{\theta\theta} - \frac{k_{z\theta}k_{\theta z}}{k_{zz}}\right)\theta + k_{xx}L^2(1 - \cos\theta)\sin\theta \quad (24)$$

Expanding the $(1-\cos\theta)\sin\theta$ in (24) by series expansion to $(1-1+\theta^2/2!-\theta^4/4!+\ldots)\cdot(\theta-\theta^3/3!+..)$ and grouping 1st order terms from (24) as $k_{\theta,tot}$, we obtain

$$M_{in} = k_{\theta,tot}\theta + \frac{1}{2!}k_{xx}L^2\theta^3 - \left(\frac{1}{2!3!}+\frac{1}{4!}\right)k_{xx}L^2\theta^5 \quad (25)$$

ACKNOWLEDGMENT

The authors would like to thank M. L. Petrovich for gift funds.

REFERENCES

[1] K. Jia, S. Pal, and H. Xie, "An electrothermal tip–tilt–piston micromirror based on folded dual S-shaped bimorphs," *J. Microelectromech. Syst.*, vol. 18, no. 5, pp. 1004–1015, Oct. 2009.

[2] W. Liao, W. Liu, Y. Zhu, Y. Tang, B. Wang, and H. Xie, "A tip-tilt-piston micromirror with symmetrical lateral-shift-free piezoelectric actuators," *IEEE Sensors J.*, vol. 13, no. 8, pp. 2873–2881, Aug. 2013.

[3] J. Choi, Z. Qiu, C.-H. Rhee, T. Wang, and K. Oldham, "A three-degree-of-freedom thin-film PZT-actuated microactuator with large out-of-plane displacement," *J. Micremech. Microeng.*, vol. 24, no. 7, Jun. 2014, Art. no. 075017.

[4] J. Choi, X. Duan, H. Li, T. Wang, and K. Oldham, "Two-photon vertical cross-sectional imaging with a thin-film lead-zirconate-titanate Z-axis microactuator," *J. Microelectromech. Syst.* to be published.

[5] C.-P.-B. Siu, H. Zeng, and M. Chiao, "Magnetically actuated MEMS microlens scanner for *in vivo* medical imaging," *Opt. Express*, vol. 15, no. 18, pp. 11154–11166, Sep. 2007.

[6] M.-H. Kiang, O. Solgaard, K. Y. Lau, and R. Müller, "Electrostatic combdrive-actuated micromirrors for laser-beam scanning and positioning," *J. Microelectromech. Syst.*, vol. 7, no. 1, pp. 27–37, Mar. 1998.

[7] C. Ataman, H. Urey, and A. Wolter, "A Fourier transform spectrometer using resonant vertical comb actuators," *J. Micromech. Microeng.*, vol. 16, no. 12, pp. 2517–2523, Oct. 2006.

[8] S. Towfighian, S. He, and R. Ben Mrad, "A low voltage electrostatic micro actuator for large out-of-plane displacement," in *Proc. ASME Int. Design Eng. Tech. Conf.*, Buffalo, NY, USA, Aug. 2014, p. 7.

[9] J. Felder, E. Lee, and D. L. DeVoe, "Large vertical displacement electrostatic zipper microstage actuators," *J. Microelectromech. Syst.*, vol. 24, no. 4, pp. 896–903, Aug. 2015.

[10] H. Li *et al.*, "Integrated monolithic 3D MEMS scanner for switchable real time vertical/horizontal cross-sectional imaging," *Opt. Express*, vol. 24, no. 3, pp. 2145–2155, Feb. 2016.

[11] G. Li *et al.*, "Visualizing epithelial expression in vertical and horizontal planes with dual axes confocal endomicroscope using compact distal scanner," *IEEE Trans. Med. Imag.*, vol. 36, no. 7, pp. 1482–1490, Jul. 2017.

[12] H. Li, X. Duan, G. Li, K. Oldham, and T. Wang, "An electrostatic MEMS translational scanner with large out-of-plane stroke for remote axial-scanning in multi-photon microscopy," *Micromachines*, vol. 8, no. 159, May 2017, Art. no. 8050159.

[13] X. Duan, H. Li, X. Li, K. Oldham, and T. Wang, "Axial beam scanning in multiphoton microscopy with MEMS-based actuator," *Opt. Express*, vol. 25, no. 3, pp. 2195–2205, Feb. 2017.

[14] S. Shaw, K. Turner, J. Rhoads, and R. Baskaran, "Parametrically excited MEMS-based filters," in *Proc. IUTAM Symp. Chaotic Dyn. Control Syst. Processes Mech.*, 2005. pp. 137–146.

[15] D. I. Caruntu and I. Martinez, "Reduced order model of parametric resonance of electrostatically actuated MEMS cantilever resonators," *Int. J. Non-Linear Mech.*, vol. 66, pp. 28–32, Nov. 2014.

[16] W. Zhang and K. L. Turner, "Application of parametric resonance amplification in a single-crystal silicon micro-oscillator based mass sensor," *Sens. Actuators A, Phys.*, vol. 122, no. 1, pp. 23–30, Jul. 2005.

[17] C. Ataman and H. Urey, "Modeling and characterization of comb-actuated resonant microscanners," *J. Micromech. Microeng.*, vol. 16, no. 1, pp. 9–16, Nov. 2006.

[18] Y. Jia, J. Yan, K. Soga, and A. A. Seshia, "Multi-frequency operation of a MEMS vibration energy harvester by accessing five orders of parametric resonance," *J. Phys., Conf. Ser.*, vol. 476, no. 1, 2013, Art. no. 012126.

[19] B. J. Gallacher, J. S. Burdess, and K. M. Harish, "A control scheme for a MEMS electrostatic resonant gyroscope excited using combined parametric excitation and harmonic forcing," *J. Microelectromech. Microeng.*, vol. 16, no. 2, pp. 320–332, Jan. 2005.

[20] W. Zhang, R. Baskaran, and K. Turner, "Tuning the dynamic behavior of parametric resonance in a micromechanical oscillator," *Appl. Phys. Lett.*, vol. 82, no. 1, pp. 130–132, Jan. 2003.

[21] B. E. DeMartini, J. F. Rhoads, K. L. Turner, S. W. Shaw, and J. Moehlis, "Linear and nonlinear tuning of parametrically excited MEMS oscillators," *J. Microelectromech. Syst.*, vol. 16, no. 2, pp. 310–318, Apr. 2007.

[22] J. F. Rhoads, S. W. Shaw, K. L. Turner, J. Moehlis, B. E. DeMartini, and W. Zhang, "Generalized parametric resonance in electrostatically actuated microelectromechanical oscillators," *J. Sound Vib.*, vols. 4–5, no. 5, pp. 797–829, Oct. 2006.

[23] M. Sharma, E. H. Sarraf, R. Baskaran, and E. Cretu, "Parametric resonance: Amplification and damping in MEMS gyroscopes," *Sens. Actuators A, Phys.*, vol. 177, pp. 79–86, Apr. 2012.

[24] S. Krylov, Y. Gerson, T. Nachmias, and U. Keren, "Excitation of large-amplitude parametric resonance by the mechanical stiffness modulation of a microstructure," *J. Micromech. Microeng.*, vol. 20, Dec. 2009, Art. no. 015041.

[25] C. Guo, E. Tatar, and G. Fedder, "Large-displacement parametric resonance using a shaped comb drive," in *Proc. IEEE Int. Conf. MEMS*, Taipei, Taiwan, Jan. 2013, pp. 173–176.

[26] W. Shahid, Z. Qiu, X. Duan, H. Li, T. Wang, and K. Oldham, "Modeling and simulation of a parametrically resonant micromirror with duty-cycled excitation," *J. Micromech. Syst.*, vol. 23, no. 6, pp. 1440–1453, Dec. 2014.

[27] M. Ozdogan, M. Daeichin, A. Ramini, and S. Towfighian, "Parametric resonance of a repulsive force MEMS electrostatic mirror," *Sens. Actuators A, Phys.*, vol. 265, no. 1, pp. 20–31, Oct. 2017.

[28] K. Moran, C. Burgner, S. Shaw, and K. Turner, "A review of parametric resonance in microelectromechanical systems," *Nonlinear Theory Appl.*, vol. 4, no. 3, pp. 198–224, 2013.

[29] Y. Xue and S. He, "A translation micromirror with large quasi-static displacement and high surface quality," *J. Micromech. Microeng.*, vol. 27, no. 1, Oct. 2016, Art. no. 015009.

[30] E. Carr, S. Olivier, and O. Solgaard, "Large-stroke self-aligned vertical comb drive actuators for adaptive optics applications," *Proc. SPIE*, vol. 6113, Jan. 2006, Art. no. 61130T.

[31] V. Milanovic, K. Castelino, and D. McCormick, "Fully-functional tip-tilt-piston micromirror array," in *Proc. IEEE/LEOS Int. Conf. Opt. MEMS Appl. Conf.*, Big Sky, MT, USA, Aug. 2006, pp. 38–39.

[32] K. Jia, S. Pal, and H. Xie, "An electrothermal tip–tilt–piston micromirror based on folded dual s-shaped bimorphs," *J. Microelectromech. Syst.*, vol. 18, no. 5, pp. 1004–1015, Oct. 2009.

[33] W. Liao, W. Liu, Y. Tang, B. Wang, and H. Xie, "Tip-tilt-piston piezoelectric micromirror with folded PZT unimorph actuators," in *Proc. IEEE Int. Conf. Nano/Micro Engineered Mol. Syst.*, Suzhou, China, Apr. 2013, pp. 969–972.

[34] J. Zhang, C. B. Teeple, J. Choi, S. Kang, J. E. Rivas, and K. R. Oldham, "Design, fabrication, and dynamics of an electromagnetic vertical microactuator for endomicroscopy," in *Proc. IEEE Int. Conf. Adv. Intell. Mechatron.*, Munich, Germany, Jul. 2017, pp. 1316–1321.

[35] Z. Qiu *et al.*, "Large displacement vertical translational actuator based on piezoelectric thin films," *J. Micromech. Microeng.*, vol. 20, no. 7, Jun. 2010, Art. no. 075016.

[36] S. Shmulevich, I. H. Grinberg, and D. Elata, "A MEMS implementation of a classic parametric resonator," *J. Microelectromech. Syst.*, vol. 24, no. 5, pp. 1285–1292, Oct. 2015.

Haijun Li received the Ph.D. degree in microelectronics and solid-state electronics from Jilin University, Changchun, China, in 2007. He held a post-doctoral position at Nanyang Technology University, Singapore, from 2008 to 2011. He was a Senior Engineer with the Hebei Semiconductor Research Institute, Shijiazhuang, China, from 1997 to 2008. He is currently a Research Investigator with the University of Michigan, Ann Arbor, MI, USA, where he is involved in the development of MEMS-based endomicroscope. His research interests include MEMS, uncooled IRFPAs, CMOS-compatible epi-MEMS micromachining, wafer level packaging, and endoscopic imaging technologies.

Paul Barnes received the B.S. degree in mechanical engineering from the University of Michigan. He works as a Structural Engineer in fracture toughness characterization and fracture stress analysis of composite aerospace materials. He previously worked as an undergraduate studying MEMS micromirror dynamics and control. He currently lives in Seattle, WA, USA, where he enjoys playing guitar and exploring the outdoors.

Eric Harding received the B.S. and M.S. degrees in mechanical engineering from the University of Michigan, with a focus on controls and medical devices.

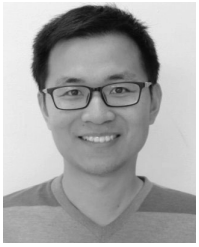

Xiyu Duan received the B.S. degree in electrical engineering from The Hong Kong University of Science and Technology in 2010 and the Ph.D. degree in biomedical engineering from the University of Michigan in 2016. His Ph.D. thesis was on MEMS-based fiber endomicroscopes to for real time optical biopsy. He is currently an Optical Engineer at Apple Inc.

Thomas D. Wang received the B.S. degree in mathematics and physics from the Harvey Mudd College and the Ph.D. degree in medical engineering and medical physics from MIT. He is currently a Professor of medicine, biomedical engineering, and mechanical engineering at the University of Michigan and the H. Marvin Pollard Collegiate Professor of Endoscopy Research. His research interests are in the field of biomedical optics, multiplexed detection, and molecular imaging. He has developed a number of microsystems-based technologies to perform scanning and actuation for high speed imaging with large working distance in endomicroscopy.

Kenn R. Oldham received the B.S. degree in mechanical engineering from Carnegie Mellon University and the Ph.D. degree in mechanical engineering from the University of California at Berkeley. He is currently an Associate Professor of mechanical engineering with the University of Michigan. His research interests include the intersection of control systems and micro-scale sensing and actuation, with interests in design for controllability, optimal and robust control, microsystem estimation and identification, and novel sensor and actuator design. Applications include terrestrial micro-robotics, endoscopic microscopy, and inertial and physiological sensing. He is a member of ASME.